AIAA JOURNAL
Vol. 36, No. 6, June 1998

Time- and Frequency-Domain Numerical Simulation of Linearized Euler Equations

Kidambi Sreenivas* and David L. Whitfield†
Mississippi State University, Mississippi State, Mississippi 39762

Linearized Euler solvers based on a high-resolution numerical scheme are presented. The approach is to linearize the numerical-flux vector as opposed to carrying through the complete linearization analysis with the dependent-variable vector written as a sum of a mean flow and a small perturbation. This allows the linearized equations to be maintained in conservation-law form in the time domain. A harmonic assumption regarding the nature of the unsteady perturbations results in a set of time-independent equations in the frequency domain. The linearized equations are used to compute unsteady flows in cascades arising from blade vibrations. The time-domain equations are solved in a time-accurate manner and the frequency-domain equations are solved using a local time-stepping procedure. Numerical solutions are compared to theoretical results, to other linearized computations, and to numerical solutions of the nonlinear Euler equations. The frequency-domain computations were found to be at least an order of magnitude faster than the corresponding time-domain computations.

Introduction

BLADE vibration (the aeroelastic problem) and noise generation (the aeroacoustic problem) are both undesirable consequences of the unsteady flow processes that occur within a turbomachine and are, therefore, important concerns to the designer. The aeroelastic problem is important because it can lead to structural failure of the blading and possibly result in extensive damage to the engine. The aeroacoustic problem, on the other hand, plays an important role in modeling sources that can be used to predict noise levels, an important consideration given the current noise-level standards at major airports, etc. An unsteady aerodynamic analysis intended for turbomachinery aeroelastic and aeroacoustic applications must be applicable over a wide range of structural geometries, mean operating conditions, and unsteady excitation modes and frequencies. Because of the large number of parameters involved, the analysis must provide the necessary unsteady information both efficiently and economically.

In an effort to be economical, many aeroacoustic and aeroelastic analyses currently rely on unsteady flowfield information that is obtained from classical methods based on rather simple potential flow models. In some cases these analyses are even based on analytical solutions of the linearized potential flow equations for two-dimensional cascades of infinitely thin blades.[1,2] More recently, there has been research directed at solving the nonlinear Euler[3–5] and Navier–Stokes[6,7] equations. The attempts at solving the nonlinear equations have been successful but prohibitively expensive. This precludes the possibility of using any of these methods in the design process.

The concept of linearized Euler analysis, introduced by Ni and Sisto,[8] is applicable to nonisentropic, rotational flows. Their work, which was limited to isentropic flows over flat-plate cascades, was extended to realistic cascade geometries by Hall and Crawley.[9] A survey of much of the work on linearized solvers, for both potential and Euler equations, is given by Verdon.[10] These approaches are based on the assumption that the unsteady flow is a perturbation of a mean flow; therefore, once a nonlinear solution is obtained for the mean flow, small perturbations of this can be studied for the conditions of interest.

Presented as Paper 93-2934 at the AIAA 24th Fluid Dynamics Conference, Orlando, FL, July 6–9, 1993; received April 30, 1997; revision received Jan. 27, 1998; accepted for publication Feb. 5, 1998.

*Postdoctoral Fellow, MSU/NSF Engineering Research Center for Computational Field Simulation, P.O. Box 9627. Member AIAA.

†Professor, MSU/NSF Engineering Research Center for Computational Field Simulation, Department of Aerospace Engineering, P.O. Box 9627. Member AIAA.

The objective of the present research is to investigate the numerical solution of a linearization of the compressible Euler equations using a high-resolution flux-difference-split scheme. The idea is to use the same numerical approach to solve both the nonlinear mean flow problem and the linearized problem. The approach is to linearize the Euler equations by a method that is based on linearizing the flux vector as opposed to carrying through the complete linearization analysis with the dependent-variable vector written as a sum of the mean and the perturbed flow. It is demonstrated that this makes for a simple and compact linearization that allows the equations to be maintained easily in conservation-law form. With the linearized equations written in conservation-law form, it is a relatively straightforward matter to apply a similar numerical flux formulation and numerical solution technique to the linearized problem as to the full nonlinear problem. In this case, a high-resolution method that is based on an approximate Riemann solver[11] is used for both the nonlinear and the linearized solutions.

The initial objective of this research was to validate the linearization technique. As a result of this, all computations were performed in the time domain. Multiple blade passages are required to simulate nonzero interblade phase angles. Newton subiterations[12] are used for time accuracy. Substantial savings in computational time were not achieved for the linearized time-domain computations because multiple Newton subiterations coupled with the use of minimum time-stepping were required to ensure time accuracy. In an effort to improve the performance of the linearized Euler solver, a transformation to the frequency domain was made. This transformation results in a set of time-independent equations that are solved, in essence, as steady-state problems for the amplitudes of the different harmonics. Furthermore, nonzero interblade phase angles can be handled using a single blade passage through the use of phase-shifted periodic boundary conditions.

Characteristic variable boundary conditions based on the linearized equations are used for the impermeable surfaces. The nonreflective boundary conditions, based on the work of Giles,[13] have been used to minimize reflections from far-field computational boundaries. Unsteady surface pressures (for the time-domain computations) were analyzed using a fast Fourier transform (FFT) as presented in Ref. 14.

The linearized equations are developed in curvilinear coordinates so as to be applicable to configurations of practical interest. A locally deforming grid is used to capture the oscillations of the cascade. Second-order accuracy in space and first-order accuracy in time are used, and the geometric conservation law (GCL) is satisfied numerically to account for deforming grids.[15,16]

Linearized results are first compared to theoretical results for cascades of infinitely thin blades oscillating in pitch and plunge. Linearized results also are compared to results obtained by other

researchers[17,18] and to nonlinear Euler solutions for loaded cascades. This demonstrates the ability of the method to capture the physics of a small-disturbance unsteady flowfield. A comparison of the CPU time required for the various computations also is presented.

Governing Equations

The two-dimensional Euler equations in conservation-law form on a dynamic, curvilinear grid are[16]

$$\frac{\partial Q}{\partial \tau} + \frac{\partial F}{\partial \xi} + \frac{\partial G}{\partial \eta} = 0 \tag{1}$$

where

$$Q = J\begin{bmatrix} \rho \\ \rho u \\ \rho v \\ e \end{bmatrix}, \qquad F = J\begin{bmatrix} \rho U \\ \rho u U + \xi_x p \\ \rho v U + \xi_y p \\ U(e+p) - \xi_t p \end{bmatrix}$$

$$G = J\begin{bmatrix} \rho V \\ \rho u V + \eta_x p \\ \rho v V + \eta_y p \\ V(e+p) - \eta_t p \end{bmatrix}$$

with

$$U = \xi_x u + \xi_y v + \xi_t, \qquad V = \eta_x u + \eta_y v + \eta_t$$

and J is the Jacobian of the inverse transformation, i.e., $J = x_\xi y_\eta - y_\xi x_\eta$. The metric quantities are given by

$$J\xi_x = y_\eta, \qquad J\eta_x = -y_\xi$$

$$J\xi_y = -x_\eta, \qquad J\eta_y = x_\xi$$

$$\xi_t = -(\xi_x x_\tau + \xi_y y_\tau), \qquad \eta_t = -(\eta_x x_\tau + \eta_y y_\tau)$$

where x_τ and y_τ are the grid velocities in the x and y directions, respectively. The system of equations in Eq. (1) is completed by the equation of state, i.e.,

$$e = [p/(\gamma - 1)] + \tfrac{1}{2}\rho(u^2 + v^2)$$

Linearized Euler Equations

For illustration purposes, consider the one-dimensional Euler equations,

$$\frac{\partial Q}{\partial \tau} + \frac{\partial F}{\partial \xi} = 0 \tag{2}$$

To start the linearization process (time domain), the flow variables can be expressed as the sum of two components, namely, a mean or steady flow component that satisfies the steady nonlinear equations, and an unsteady perturbation, i.e.,

$$Q = \bar{Q} + Q' \tag{3}$$

where the perturbation variables Q' are small compared to their mean flow counterparts $\bar{Q}$. Similarly, the flux can be viewed as composed of two components, i.e.,

$$F = \bar{F} + F' \tag{4}$$

Using Eqs. (3) and (4) in Eq. (2) and noting that the mean flow satisfies

$$\frac{\partial \bar{Q}}{\partial \tau} + \frac{\partial \bar{F}}{\partial \xi} = 0$$

yields

$$\frac{\partial Q'}{\partial \tau} + \frac{\partial F'}{\partial \xi} = 0 \tag{5}$$

Equation (5) is the one-dimensional linearized Euler equation in the time domain. This approach can be extended to multiple dimensions, resulting in

$$\frac{\partial Q'}{\partial \tau} + \frac{\partial F'}{\partial \xi} + \frac{\partial G'}{\partial \eta} = 0 \tag{6}$$

Table 1 Summary of variables for various governing equations

Governing equation	$\mathcal{Q}$	$\mathcal{F}$	$\mathcal{G}$	$\mathcal{S}$
Nonlinear (time domain)	Q	F	G	Φ
Linearized (time domain)	Q'	F'	G'	Φ
Linearized (frequency domain)	Q_0	F_0	G_0	$-i\omega Q_0$

To obtain the linearized Euler equations in the frequency domain, the unsteady perturbations are assumed to be harmonic, i.e.,

$$Q' = \mathrm{Re}\{Q_0 \exp(i\omega\tau)\}, \qquad F' = \mathrm{Re}\{F_0 \exp(i\omega\tau)\}$$
$$G' = \mathrm{Re}\{G_0 \exp(i\omega\tau)\} \tag{7}$$

where $\mathrm{Re}\{\cdot\}$ = Real part of $\{\cdot\}$, ω = fundamental frequency of excitation, $(\cdot)_0$ = complex amplitude of $(\cdot)'$, and $i = \sqrt{-1}$.

Using Eq. (7) in Eq. (6) and noting that $\exp(i\omega\tau) \neq 0$ results in

$$i\omega Q_0 + \frac{\partial F_0}{\partial \xi} + \frac{\partial G_0}{\partial \eta} = 0 \tag{8}$$

Equation (8) is independent of time and represents a steady-state problem. Consequently, solution acceleration techniques such as local time-stepping and multigrid methods can be used to speed up the solution process. In practice, Eq. (8) is solved by adding a pseudotime derivative and driving this time derivative to zero; i.e., the governing equation used in the actual solution process is

$$\frac{\partial Q_0}{\partial \tau} + i\omega Q_0 + \frac{\partial F_0}{\partial \xi} + \frac{\partial G_0}{\partial \eta} = 0 \tag{9}$$

Equations (1), (6), and (9) can be represented in an unified manner as

$$\frac{\partial \mathcal{Q}}{\partial \tau} + \frac{\partial \mathcal{F}}{\partial \xi} + \frac{\partial \mathcal{G}}{\partial \eta} = \mathcal{S} \tag{10}$$

Table 1 provides a summary of the various governing equations and the choice of the variables that result in the same. In Table 1, Φ represents the null vector.

Numerical Formulas for F'

F' is, by definition, a perturbation of the flux. Depending on the numerical flux formulations used for the total flux, this perturbation can have different forms. The approach here is based on Roe's[19] flux difference splitting.

A first-order-accurate numerical flux difference based on Roe's flux-difference-splitting approach can be written as

$$\delta F = F_R - F_L = JA(q_R, q_L, M_\xi)(q_R - q_L)$$

where the subscripts R and L refer to the right and left of an interface, respectively; $A(q_R, q_L, M_\xi)$ is the Roe-averaged flux Jacobian; and q is the Cartesian dependent-variable vector ($[\varrho, \varrho u, \varrho v, e]^T$). The added dependence of A on M_ξ (the vector of metrics) is due to the transformation to curvilinear coordinates. Expanding in a Taylor series about the mean flow quantities yields

$$\delta F = \delta \bar{F} + J'A(\bar{q}_R, \bar{q}_L, \bar{M}_\xi)(\bar{q}_R - \bar{q}_L) + \bar{J}A(\bar{q}_R, \bar{q}_L, \bar{M}_\xi)(q'_R - q'_L) + \epsilon \tag{11}$$

where ϵ, the error in the linearization, is given by

$$\epsilon = \bar{J}\frac{\partial A}{\partial q_R}\bigg|_{\bar{q}_R, \bar{q}_L, \bar{M}_\xi} q'_R(\bar{q}_R - \bar{q}_L) + \bar{J}\frac{\partial A}{\partial q_L}\bigg|_{\bar{q}_R, \bar{q}_L, \bar{M}_\xi} q'_L(\bar{q}_R - \bar{q}_L) + \bar{J}\frac{\partial A}{\partial M_\xi}\bigg|_{\bar{q}_R, \bar{q}_L, \bar{M}_\xi} M'_\xi(\bar{q}_R - \bar{q}_L) + \mathcal{O}\left(q'^2, M'^2_\xi\right)$$

and

$$\delta \bar{F} = \bar{J}A(\bar{q}_R, \bar{q}_L, \bar{M}_\xi)(\bar{q}_R - \bar{q}_L)$$

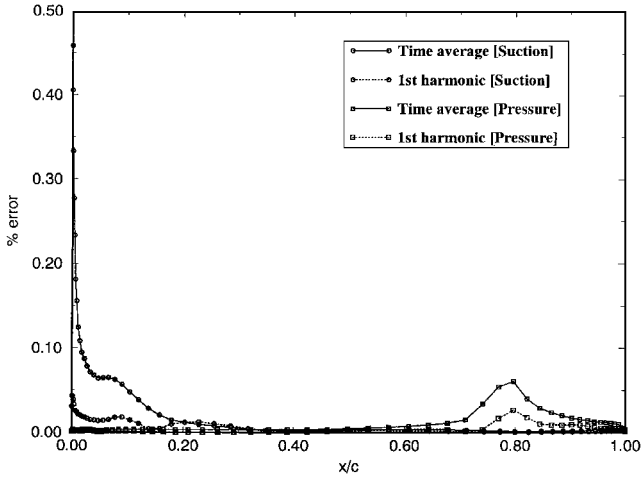

a) Subsonic case

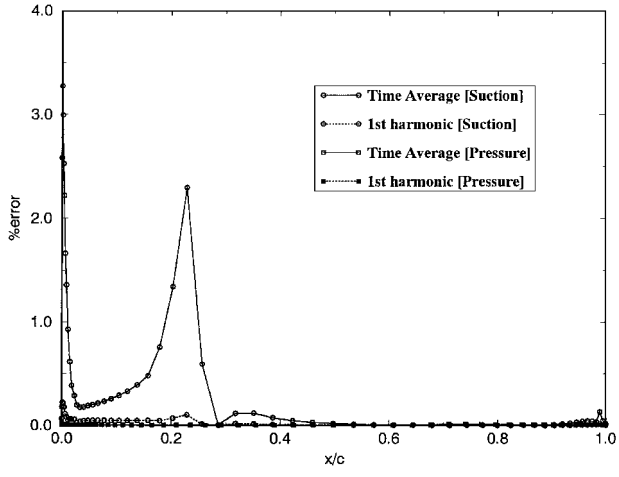

b) Transonic case

Fig. 1 Error in approximating flux differences.

This approximation is similar to the one considered by Barth,[20] though in that case, the linearization was with respect to time. From Eq. (11), observe that for a constant state vector $\bar{Q}$ (uniform mean flow), the error involves only the second-order terms, which are negligible under the small-perturbation assumption. In the case of a nonuniform mean flow, the error is modulated by $\|\Delta\bar{q}\|$. Therefore, if the gradients are not too large, the error is still small. This is reflected in Fig. 1a, which shows the chordwise distribution of relative error (percent), defined as

$$\%\ \text{error} = \frac{\|\epsilon\|_\infty}{\|\delta F\|_\infty} \times 100, \qquad \|\cdot\|_\infty \equiv \text{infinity norm}$$

for a subsonic mean flow condition ($M_\infty = 0.7$; $\alpha = 10$ deg). The relative error in Fig. 1 is calculated on the basis of streamwise flux difference for a cascade of airfoils (Tenth Standard Configuration[21]) vibrating in plunge at a semichord reduced frequency κ of 0.6435 and an interblade phase angle σ of zero. The chordwise distribution of the relative error when sharp gradients are present (shock in blade passage, $M_\infty = 0.8$; $\alpha = 13$ deg) is shown in Fig. 1b. In this case, the error is higher than for the subsonic case, but is still within acceptable limits. Based on this analysis, a form for the perturbed flux difference can be defined as

$$\delta F' = F'_R - F'_L = \bar{J}A(\bar{q}_R, \bar{q}_L, \bar{M}_\xi)(Q'_R - Q'_L)$$

where

$$Q'_R = (J'/\bar{J})\bar{q}_R + q'_R, \qquad Q'_L = (J'/\bar{J})\bar{q}_L + q'_L$$

The flux at any face then can be calculated as

$$F'_{i+\frac{1}{2}} = F'_L + \sum\nolimits^{-} \alpha'_j \bar{\lambda}^{(j)} \bar{r}^{(j)} \tag{12}$$

where

α'_j = strength of the jth wave $= \bar{l}^{(j)} \cdot dQ'$
$\bar{\lambda}^{(j)}$ = jth eigenvalue of $A(\bar{q}_R, \bar{q}_L, \bar{M}_\xi)$
$\bar{l}^{(j)}, \bar{r}^{(j)}$ = jth left and right eigenvectors of $A(\bar{q}_R, \bar{q}_L, \bar{M}_\xi)$, respectively
dQ' = $Q'_R - Q'_L$

and $\sum^-$ denotes summation over the negative wave speeds.

The calculation of the perturbed flux at any interface involves the computation of F'_L. The form of F'_L can be obtained through a linearization of the flux vector; i.e., expanding F_L [from Eq. (1)] in a Taylor series about the mean flow quantities and neglecting higher-order terms results in

$$F'_L = \tilde{A}(\bar{q}_L, \bar{M}_\xi)Q'_L + R(\bar{Q}_L, \bar{M}_\xi)M'_\xi \tag{13}$$

where

$$\tilde{A}(\bar{q}_L, \bar{M}_\xi) = \left.\frac{\partial F}{\partial q}\right|_{\bar{q}_L, \bar{M}_\xi}, \qquad R(\bar{Q}_L, \bar{M}_\xi) = \left.\frac{\partial F}{\partial M_\xi}\right|_{\bar{Q}_L, \bar{M}_\xi}$$

The flux formulas for the frequency-domain computations can be obtained by using Eq. (7) in Eqs. (12) and (13); i.e.,

$$F_{0_{i+\frac{1}{2}}} = F_{0L} + \sum\nolimits^{-} \alpha_{0j} \bar{\lambda}^{(j)} \bar{r}^{(j)} \tag{14}$$

and

$$F_{0L} = \tilde{A}(\bar{q}_L, \bar{M}_\xi)Q_{0L} + R(\bar{Q}_L, \bar{M}_\xi)M_{0\xi} \tag{15}$$

where

α_{0j} = strength of the jth wave $= \bar{l}^{(j)} \cdot dQ_0$
$\bar{\lambda}^{(j)}$ = jth eigenvalue of $A(\bar{q}_R, \bar{q}_L, \bar{M}_\xi)$
$\bar{l}^{(j)}, \bar{r}^{(j)}$ = jth left and right eigenvectors of $A(\bar{q}_R, \bar{q}_L, \bar{M}_\xi)$, respectively
dQ_0 = $Q_{0R} - Q_{0L}$
M'_ξ = $\mathrm{Re}\{M_{0\xi} \exp(i\omega\tau)\}$

A drawback of Eqs. (12) and (14) is that they are only of first-order spatial accuracy. Higher-order spatial accuracy in the time-domain computations are obtained using the methods described in Ref. 11, and limiters are used to control oscillations. The frequency-domain computations do not use limiters and simple flux extrapolation is used to obtain higher-order accuracy. All of the results presented here are second-order accurate in space.

Numerical Formulation

An implicit, finite volume semidiscretization of Eq. (10) may be written as

$$\frac{\partial \mathcal{Q}_{ij}}{\partial \tau} = -\mathfrak{R} \tag{16}$$

where

$$\mathfrak{R} = \delta_i \mathcal{F} + \delta_j \mathcal{G} - \mathcal{S}$$

$$\delta_*(\cdot) = (\cdot)_{*+\frac{1}{2}} - (\cdot)_{*-\frac{1}{2}}$$

where i, j denotes a finite volume (cell) center and $* \pm \frac{1}{2}$ denotes a cell interface. The following difference expression, encompassing a broad class of difference representations, was used for advancing the solution of Eq. (16) in time:

$$\frac{(1+\psi)\Delta\mathcal{Q}^n - \psi\Delta\mathcal{Q}^{n-1}}{\Delta\tau} = (\theta - 1)\mathfrak{R}^n - \theta\mathfrak{R}^{n+1}$$
$$\Delta\mathcal{Q}^n = \mathcal{Q}^{n+1} - \mathcal{Q}^n \tag{17}$$

Specializing Eq. (17) for the various cases and applying Newton's method[12] to the resulting equations yields the system of equations that need to be solved. The GCL is satisfied numerically during this formulation process. For the frequency-domain computations and for obtaining the mean flow, only one Newton subiteration is used.[22] First-order accuracy in time has been exclusively used in this study for the linearized equations whereas the nonlinear equations are solved using second-order accuracy in time.

Numerical Solution Method

The system of equations resulting from the application of Newton's method can be written as

$$(L + D + U)x = b \tag{18}$$

where L is strictly lower block triangular, D is block diagonal, and U is strictly upper block triangular. The system defined by Eq. (18) is solved using the N-Pass algorithm. The N-Pass algorithm can be viewed as a relaxation scheme based on the symmetric Gauss–Seidel algorithm. It can be represented as

$$\left.\begin{aligned}(L + D)x^{2N-1} + Ux^{2N-2} &= b\\ (D + U)x^{2N} + Lx^{2N-1} &= b\end{aligned}\right\}, \qquad N \geq 1$$

where N is the number of the current iteration and $x^0 = 0$. The 4×4 system at every grid point is solved using Doolittle's method.[23]

Boundary Conditions

Solid Surface

Characteristic variable boundary conditions are used for the steady as well as the unsteady nonlinear Euler computations. Details of this method are available elsewhere in the literature[24,25] and are not repeated here. The boundary conditions for the linearized equations are based on a linearization of the characteristic variables. A linearized version of the flow tangency condition is satisfied at the impermeable surface.[26] For the frequency-domain computations, the boundary conditions take into account the presence of the source term. This is handled using the method outlined in Ref. 27.

Far-Field Conditions

The formulation and implementation of far-field conditions for steady flows is identical to that used in Ref. 24. The unsteady inflow and outflow (subsonic) boundary conditions are based on the work of Giles[13] and the details of implementation are given in Ref. 28.

Periodic Boundary Conditions

The boundaries that extend upstream and downstream of the airfoils are called periodic boundaries for airfoils with harmonic motion and specified interblade phase angle. For the time-domain computations, injection of dependent variables is used to specify the boundary condition for a given blade passage, and multiple blade passages are used to satisfy the periodicity condition.[26] For the frequency-domain case, phase-shifted boundary conditions are used, thereby alleviating the need for multiple blade passages.[22] This leads directly to substantial savings in computational time.

Results

As a part of the code validation process, linearized results are first compared with linear theory for a cascade of flat plates oscillating in plunge as well as pitch for different cascade geometries and freestream conditions. Linearized Euler results also are compared with nonlinear Euler solutions and to linearized results from other researchers for a cascade of airfoils, for which no theoretical results are available. The cases considered here involved a cascade undergoing plunging or pitching motion defined as

$$\left.\begin{aligned}\alpha &= \hat{\alpha}\cos(\omega\tau + m\sigma)\\ h &= \hat{h}\cos(\omega\tau + m\sigma)\end{aligned}\right\}, \qquad m = 0, 1, 2, 3, \ldots, M - 1$$

where $\hat{\alpha}$ and $\hat{h}$ are the amplitudes of pitching and plunging motions, respectively; ω is the frequency; σ is the interblade phase angle; and τ is the time. M is the number of blade rows required to impose a periodicity condition. All of the results presented here are normalized by respective amplitudes of pitch or plunge, as the case may be.

Time-domain computations were carried out using 200 time steps per period of motion (with two Newton subiterations per time step) and needed three to four periods to reach a periodic state. An FFT based on Ref. 14 has been used to decompose the time-varying pressure at any given point into real and imaginary parts of the complex amplitudes of the various harmonics. The frequency-domain results typically required a total of 200 time steps (with no subiterations) to reach a converged state. All of the results shown here are for the first harmonic. A schematic of a typical two-dimensional cascade defining the various terms used in this section is shown in Fig. 2.

Table 2 Summary of uniform mean-flow test cases

Test case	Gap-to-chord ratio	Stagger angle, deg	Freestream Mach number
1	0.311	28	2.61
2	1.0	0	0.5

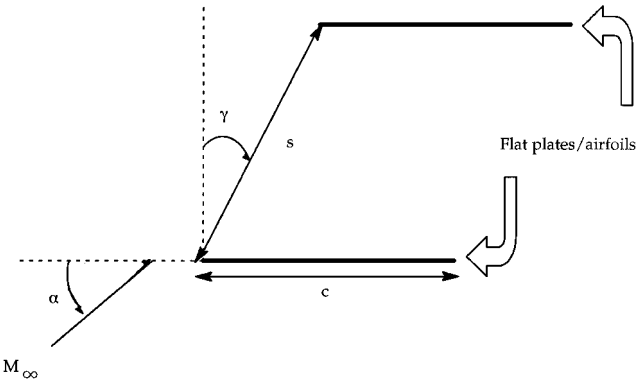

Fig. 2 Schematic of typical cascade: c = chord length; s = gap; s/c = gap to chord ratio; γ = stagger angle; α = angle of attack; M_∞ = freestream Mach number.

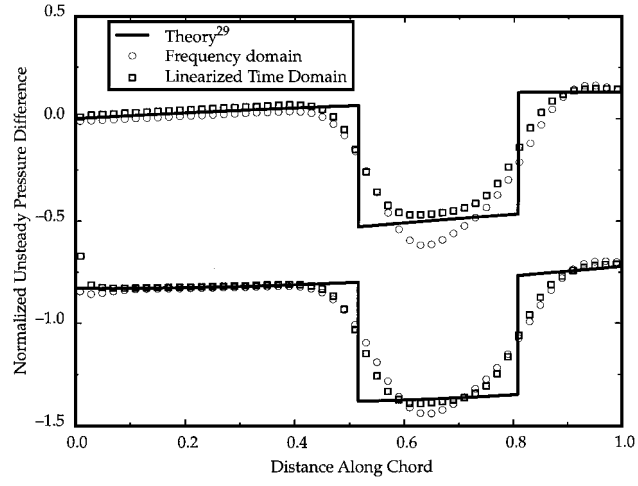

Fig. 3 Unsteady pressure difference on a flat-plate cascade due to plunging motion ($M_\infty = 2.61$, $s/c = 0.311$, $\gamma = 28$ deg, $\kappa = 0.5$, and $\sigma = 90$ deg).

Unsteady Flow in a Flat-Plate Cascade

In an effort to validate the linearized Euler solver, a number of unsteady flows about a cascade of infinitely thin flat-plate airfoils were computed and compared to linear theory.[29,30] For all the cases considered in this section, the mean flow through the cascade is uniform, i.e., $\alpha = 0$ deg. All computations were performed on a 71×51 H-grid (with 50 points each on the suction and pressure sides). Two different cascade geometries and freestream conditions were considered for the validation, and their characteristic features are summarized in Table 2.

Linearized results are compared first to available theoretical results for the first test case. The cascade is oscillating in plunge at a reduced frequency (based on semichord) of 0.5 and an interblade phase angle of 90 deg. The Courant–Friedrichs–Lewy (CFL) was 5 (maximum CFL) for the time-domain computations and 15 for the frequency-domain computations. As can be seen from Fig. 3, the overall agreement between the theoretical and computed results is fair. The location as well as the strength of the real and imaginary parts of the discontinuities are captured accurately by the linearized time-domain solver. The overshoots experienced by the frequency-domain computations are attributed to the lack of flux limiters coupled with the fact that the mean flow does not contain any

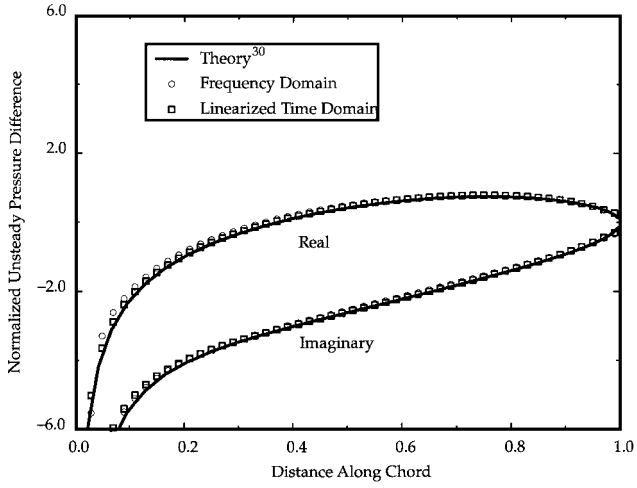

Fig. 4 Unsteady pressure difference on a flat-plate cascade due to plunging motion ($M_\infty = 0.5, s/c = 1.0, \gamma = 0$ deg, $\kappa = 0.5$, and $\sigma = 180$ deg).

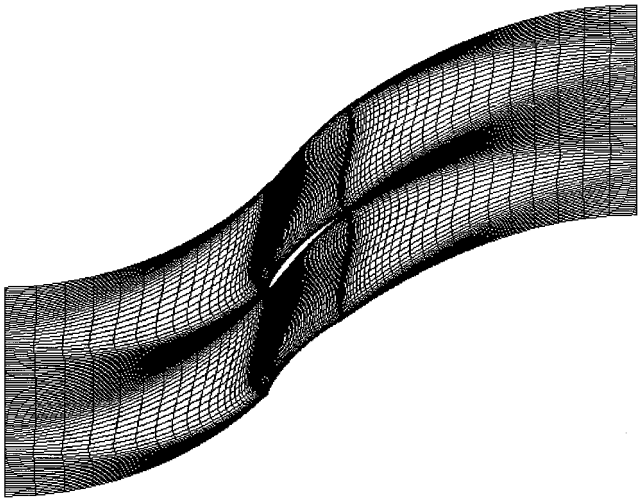

Fig. 5 Cascade geometry and multiblock grid used in computation.

discontinuities. Time- and frequency-domain results also are compared to linear theory for the second test case. The cascade is oscillating in plunge at a semichord reduced frequency of 0.5 and an interblade phase angle of 180 deg. The CFL was 15 for the frequency-domain computations, whereas a maximum CFL of 5 was employed for the corresponding time-domain results. As can be seen from Fig. 4, the agreement between the theoretical and the computed results is good.

Unsteady Flow in an Airfoil Cascade

Having demonstrated the ability of the linearized solver to accurately predict unsteady pressures for subsonic and supersonic flat-plate cascades, consideration is now given to a more realistic cascade geometry. The cascade chosen for this study is the so-called Tenth Standard Configuration,[21] which is a cascade consisting of modified NACA 0006 airfoils. The gap-to-chord ratio is 1.0 and the stagger angle is 45 deg. Two distinct flow regimes are used to demonstrate the high-resolution nature of the linearized solvers. The first is a subsonic cascade ($M_\infty = 0.7, \alpha = 10$ deg) and the second a transonic case ($M_\infty = 0.8, \alpha = 13$ deg). The transonic case is characterized by a shock in the blade passage. The mean flow through the cascade is no longer uniform and is computed by solving the nonlinear Euler equations using a time-marching algorithm with local time stepping to speed up convergence. The cascade geometry and the grid used in the computation are shown in Fig. 5. The steady pressure distributions for the two cases are shown in Figs. 6 and 7. The maximum CFL used in the time-domain calculations was 85 for the subsonic case and 80 for the transonic case; a CFL of 15 was used for the frequency-domain computations.

As part of the validation of the linearized formulations presented here, results from the time- and frequency-domain computations

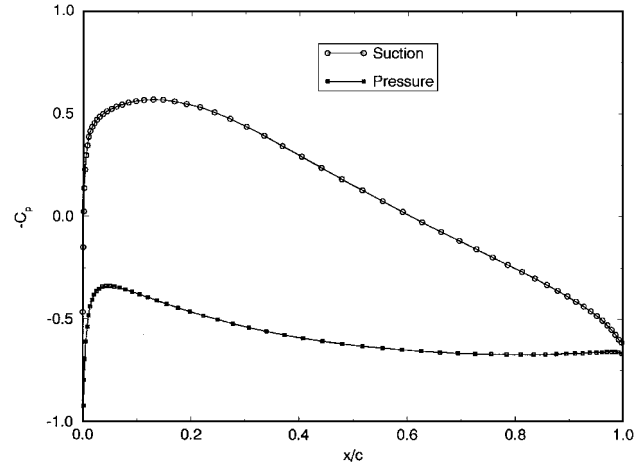

Fig. 6 Steady pressure distribution for subsonic Tenth Standard Configuration cascade.

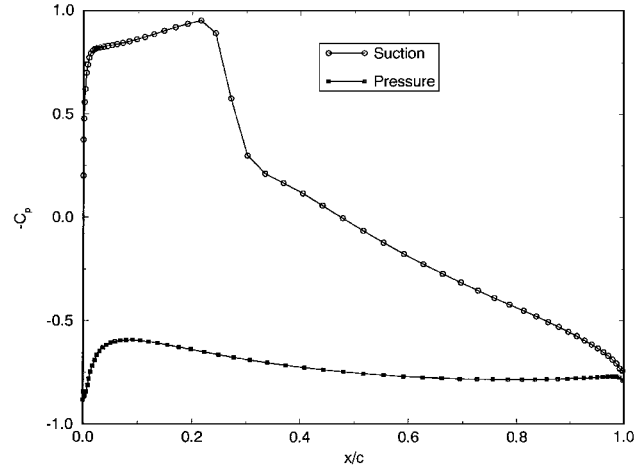

Fig. 7 Steady pressure distribution for transonic Tenth Standard Configuration cascade.

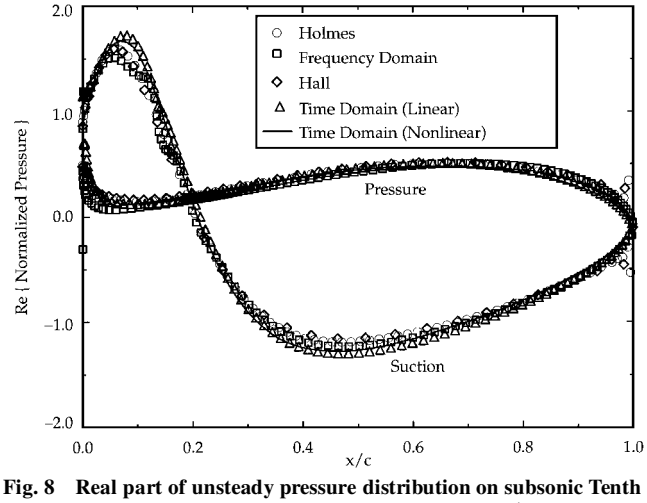

Fig. 8 Real part of unsteady pressure distribution on subsonic Tenth Standard Configuration cascade due to plunging motion ($\kappa = 1.0$ and $\sigma = 0$ deg).

are compared to linearized results obtained by Kenneth Hall and Graham Holmes and to nonlinear computations. A 161×49 H-grid, with 100 points each on the pressure and suction surfaces, was used to compute the results obtained using the formulations presented here.

The first test case involves the subsonic cascade oscillating in plunge at a reduced frequency of 1.0 and an interblade phase angle of 0 deg. The real and imaginary parts of the unsteady pressure distribution are shown in Figs. 8 and 9, respectively. Also included in these figures are results obtained by solving the nonlinear Euler equations for the same flow conditions. As can be seen from these

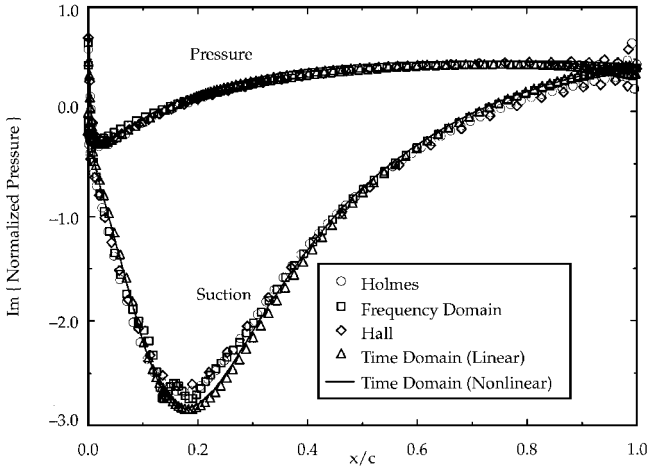

Fig. 9 Imaginary part of unsteady pressure distribution on subsonic Tenth Standard Configuration cascade due to plunging motion (κ = 1.0 and σ = 0 deg).

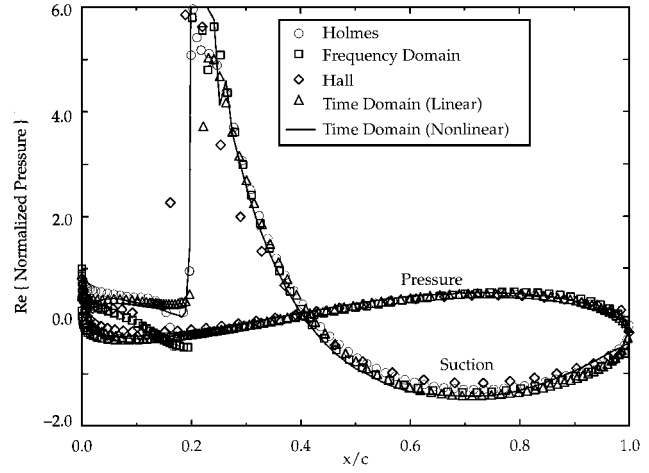

Fig. 10 Real part of unsteady pressure distribution on transonic Tenth Standard Configuration cascade due to pitching motion (κ = 1.0 and σ = 0 deg).

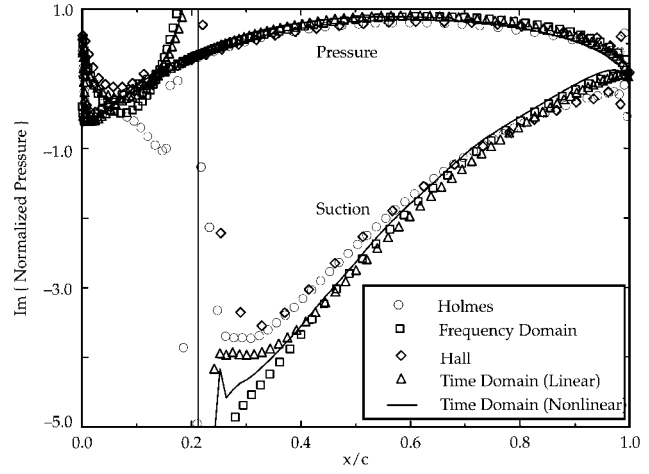

Fig. 11 Imaginary part of unsteady pressure distribution on transonic Tenth Standard Configuration cascade due to pitching motion (κ = 1.0 and σ = 0 deg).

two figures, the agreement between the nonlinear and the linearized solutions is very good.

The second test case involves the transonic cascade oscillating in pitch at a reduced frequency of 1.0 and an interblade phase angle of 0 deg. The pitching axis is located at 0% chord; i.e., the cascade is pitching about the leading edge. As can be seen from Fig. 10 (real part) and Fig. 11 (imaginary part), the agreement between the various linearized computations is good. The high-resolution nature of the linearized solver presented here is evident from the crisp resolution of the discontinuities. The linearized computations compare favorably with the nonlinear computations.

The differences between the time- and frequency-domain computations (in Figs. 8–11) are attributed to the lack of flux limiting in the frequency domain. Results obtained using second-order accuracy in time for the linearized time-domain computations (not shown) were not significantly different from the first-order results shown here. In an effort to determine the range of amplitudes over which the linearized analysis would be valid, the nonlinear computations were performed using amplitudes ranging from 1/10,000 of a chord to 2/10 of a chord. It was found that amplitudes beyond one-tenth of a chord resulted in significant nonlinear effects.

Results from the linearized formulations presented here are compared to nonlinear computations and linearized results obtained by Hall and Clark[17] (digitized from Ref. 17) for nonzero interblade phase angles. A 121×41 grid, with 60 points each on the pressure and suction surfaces, was used for the computations. The two cases considered involve the Tenth Standard Configuration cascade oscillating in plunge at a reduced frequency of 0.6435 and an interblade phase angle of -90 deg. The real and imaginary parts of the first harmonic of the unsteady pressure distribution are shown in Figs. 12 and 13 (subsonic case) and in Figs. 14 and 15 (transonic case), respectively. As can be seen from these figures, the agreement between the linearized and the nonlinear solutions is good.

Performance of Linear vs Nonlinear Solvers

Table 3 compares the time required to converge a frequency-domain computation (requiring 200 time steps) with the time

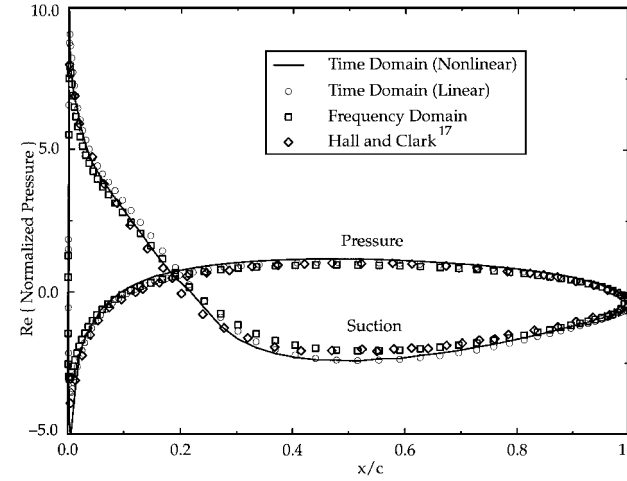

Fig. 12 Real part of unsteady pressure distribution on subsonic Tenth Standard Configuration cascade due to plunging motion (κ = 0.6435 and σ = $-$90 deg).

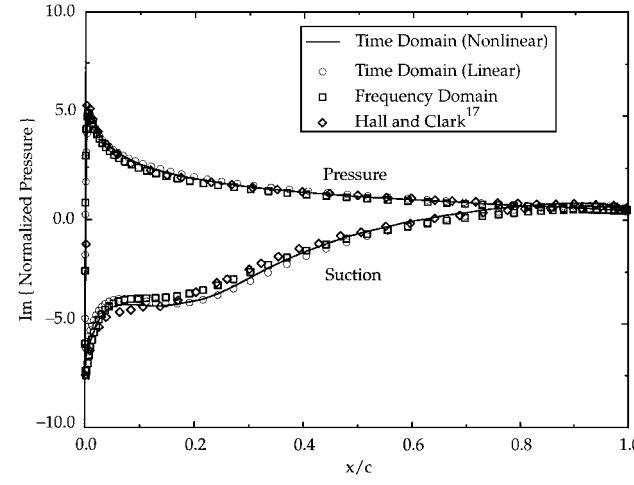

Fig. 13 Imaginary part of unsteady pressure distribution on subsonic Tenth Standard Configuration cascade due to plunging motion (κ = 0.6435 and σ = $-$90 deg).

Table 3 Relative performance of nonlinear and linearized solvers

Type of solver	Cray CPU time, s
Time domain (nonlinear)	300
Time domain (linearized)	210
Frequency domain	60

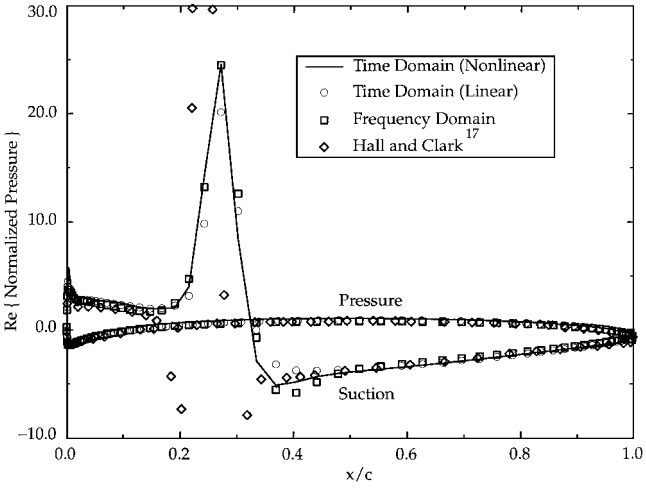

Fig. 14 Real part of unsteady pressure distribution on transonic Tenth Standard Configuration cascade due to plunging motion (κ = 0.6435 and σ = −90 deg).

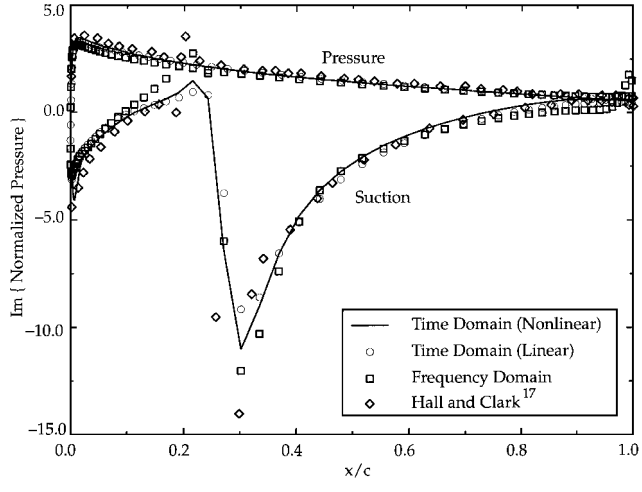

Fig. 15 Imaginary part of unsteady pressure distribution on transonic Tenth Standard Configuration cascade due to plunging motion (κ = 0.6435 and σ = −90 deg).

required to achieve a periodic solution (requiring two Newton subiterations per time step and four cycles of blade vibration) using the linearized and nonlinear (both time domain) formulations. The comparisons are for a one block, 121×41 grid. As can be seen from the time taken, the frequency-domain solver is about 500% faster than the nonlinear solver. In the case of nonzero interblade phase angle, the time-domain computation time is effectively multiplied by the number of blocks, whereas the frequency-domain numbers are relatively unaffected. Therefore, even more significant speedups can be achieved for out-of-phase computations using the frequency-domain approach over the time-domain approaches.

Conclusions

Linearized Euler solvers based on a high-resolution flux-difference-split scheme are presented. The linearized equations are maintained in conservation-law form and the same solution procedure is used to solve the nonlinear steady as well as the linearized equations. The computed results are in good agreement with theoretical results for flat-plate cascades and with nonlinear and other linearized computations for airfoil cascades over all flow regimes. The frequency-domain approach is significantly faster than the time-domain approaches.

Acknowledgments

This work is supported by the NASA Lewis Research Center, grant NAG-3-767, with Dennis Huff as Technical Monitor. The authors are also grateful to Kenneth Hall of Duke University and Graham Holmes of General Electric R&D Center for providing the solutions for comparison purposes. The authors wish to express their thanks to John Adamczyk of NASA Lewis Research Center for the idea that started it all. Computer time for the Cray Y-MP was provided by NASA Lewis Research Center.

References

[1] Lane, F., "Supersonic Flow Past an Oscillating Cascade with Supersonic Leading Edge Locus," *Journal of the Aeronautical Sciences*, Vol. 24, Jan. 1957, pp. 65, 66.

[2] Whitehead, D. S., "Classical Two-Dimensional Methods," *AGARD Manual on Aeroelasticity in Axial-Flow Turbomachines*, Vol. 1, edited by M. F. Platzer and F. O. Carta, AGARD AG-298, 1987, Chap. 3.

[3] He, L., "An Euler Solution for Unsteady Flows Around Oscillating Blades," 34th International Gas Turbine and Aeroengine Congress and Exhibition, ASME Paper 89-GT-279, Toronto, ON, Canada, June 1989.

[4] Huff, D. L., Swafford, T. W., and Reddy, T. S. R., "Euler Flow Predictions for an Oscillating Cascade Using a High-Resolution Wave-Split Scheme," 36th International Gas Turbine and Aeroengine Congress and Exposition, ASME Paper 91-GT-198, Orlando, FL, June 1991.

[5] Reddy, T. S. R., Bakhle, M. A., Huff, D. L., and Swafford, T. W., "Analysis of Cascades Using a Two-Dimensional Euler Aeroelastic Solver," AIAA Paper 92-2370, April 1992.

[6] Huff, D. L., "Numerical Analysis of Flow Through Oscillating Cascade Sections," AIAA Paper 89-0437, Jan. 1989.

[7] Giles, M., and Haimes, R., "Validation of a Numerical Method for Unsteady Flow Calculations," 36th International Gas Turbine and Aeroengine Congress and Exposition, ASME Paper 91-GT-271, Orlando, FL, June 1991.

[8] Ni, R. H., and Sisto, F., "Numerical Computation of Nonstationary Aerodynamics of Flat Plate Cascades in Compressible Flow," *Journal of Engineering for Power*, Vol. 98, April 1976, pp. 165–170.

[9] Hall, K. C., and Crawley, E. F., "Calculation of Unsteady Flows in Turbomachinery Using the Linearized Euler Equations," *AIAA Journal*, Vol. 27, No. 6, 1989, pp. 777–787.

[10] Verdon, J. M., "Unsteady Aerodynamic Methods for Turbomachinery Aeroelastic and Aeroacoustic Applications," AIAA Paper 92-0011, Jan. 1992.

[11] Whitfield, D. L., Janus, J. M., and Simpson, L. B., "Implicit Finite Volume High Resolution Wave-Split Scheme for Solving the Unsteady Three Dimensional Euler and Navier–Stokes Equations on Stationary or Dynamic Grids," Mississippi State Engineering and Industrial Research Station, Rept. MSSU-EIRS-ASE-99-2, Mississippi State, MS, Feb. 1988.

[12] Whitfield, D. L., and Taylor, L., "Discretized Newton-Relaxation Solution of High Resolution Flux–Difference Split Schemes," AIAA Paper 91-1539, June 1991.

[13] Giles, M., "Non-Reflecting Boundary Conditions for Euler Equation Calculations," *Proceedings of the AIAA 9th Computational Fluid Dynamics Conference* (Buffalo, NY), AIAA, Washington, DC, 1989, pp. 143–153 (AIAA Paper 89-1942).

[14] Singleton, R. C., "An Algorithm for Computing the Mixed Radix Fast Fourier Transform," *IEEE Transactions on Audio and Electroacoustics*, Vol. 17, June 1969, pp. 93–103.

[15] Thomas, P. D., and Lombard, C. K., "Geometric Conservation Law and Its Applications to Flow Computations on Moving Grids," *AIAA Journal*, Vol. 17, No. 10, 1979, pp. 1030–1037.

[16] Janus, J. M., "Advanced 3-D CFD Algorithm for Turbomachinery," Ph.D. Dissertation, Dept. of Aerospace Engineering, Mississippi State Univ., Mississippi State, MS, May 1989.

[17] Hall, K. C., and Clark, W. S., "Prediction of Unsteady Aerodynamic Loads in Cascades Using the Linearized Euler Equations," AIAA Paper 91-3378, June 1991.

[18] Holmes, D. G., and Chuang, H. A., "2D Linearized Harmonic Euler Flow Analysis for Flutter and Forced Response," *Unsteady Aerodynamics, Aeroacoustics, and Aeroelasticity of Turbomachines and Propellers*, edited by H. M. Atassi, Springer–Verlag, New York, 1993, pp. 213–230.

[19] Roe, P. L., "Approximate Riemann Solvers, Parameter Vector, and Difference Schemes," *Journal of Computational Physics*, Vol. 43, No. 7, 1981, pp. 357–372.

[20] Barth, T. J., "Analysis of Implicit Local Linearization Techniques for Upwind and TVD Algorithms," AIAA Paper 87-0595, Jan. 1987.

[21]Bolcs, A., and Fransson, T. H., "Aeroelasticity in Turbomachines: Comparison of Theoretical and Experimental Cascade Results," U.S. Air Force Office of Scientific Research, AFOSR-TR-87-0605, Washington, DC, 1986.

[22]Sreenivas, K., "Linearized Euler Analysis of Turbomachinery," Ph.D. Dissertation, Dept. of Aerospace Engineering, Mississippi State Univ., Mississippi State, MS, Dec. 1996.

[23]Dahlquist, G., and Bjorck, A., *Numerical Methods*, Prentice–Hall, Englewood Cliffs, NJ, 1974, pp. 156–158.

[24]Whitfield, D. L., and Janus, J. M., "Three-Dimensional Unsteady Euler Equations Solution Using Flux Vector Splitting," AIAA Paper 84-1552, June 1984.

[25]Belk, D. M., "Unsteady Three-Dimensional Euler Equations Solutions on Dynamic Blocked Grids," Ph.D. Dissertation, Mississippi State Univ., Mississippi State, MS, 1986.

[26]Sreenivas, K., "High Resolution Numerical Simulation of the Linearized Euler Equations in Conservation Law Form," M.S. Thesis, Dept. of Aerospace Engineering, Mississippi State Univ., Mississippi State, MS, Aug. 1993.

[27]Kisielewski, K. M., "A Numerical Investigation of Rain Effects on Lift Using a Three-Dimensional Split Flux Vector Form," M.S. Thesis, Dept. of Aerospace Engineering, Mississippi State Univ., Mississippi State, MS, May 1985.

[28]Huff, D. L., "Pressure Wave Propagation Studies for Oscillating Cascades," AIAA Paper 92-0145, Jan. 1992.

[29]Ramsey, J. K., and Kielb, R. E., "A Computer Program for Calculating Unsteady Aerodynamic Coefficients for Cascades in Supersonic Axial Flow," NASA TM 100204 (corrected version), 1987.

[30]Smith, S. N., "Discrete Frequency Sound Generation in Axial Flow Turbomachines," Engineering Dept., Cambridge Univ., TR CUED/A-Turbo/TR 29, Cambridge, England, UK, 1971.

J. Kallinderis
Associate Editor